Astronomy & Astrophysics manuscript no. MRC0943-242
October 14, 2015
©ESO 2015

arXiv:1510.03442v1 [astro-ph.GA] 12 Oct 2015

The Mysterious Morphology of MRC0943-242 as Revealed by ALMA and MUSE

Bitten Gullberg[1], Carlos De Breuck[1], Matthew D. Lehnert[2], Joël Vernet[1], Roland Bacon[3], Guillaume Drouart[4], Bjorn Emonts[5], Audrey Galametz[6], Rob Ivison[1,7], Nicole P. H. Nesvadba[8], Johan Richard[3], Nick Seymour[9], Daniel Stern[10], and Dominika Wylezalek[11]

[1] European Southern Observatory, Karl-Schwarzschild-Str. 2, D-85748 Garching
e-mail: bgullber@eso.org
[2] Institut d'Astrophysique de Paris, UMR 7095, CNRS, Université Pierre et Marie Curie, 98bis boulevard Arago, 75014, Paris, France
[3] CRAL, Observatoire de Lyon, CNRS, Université Lyon 1, 9 avenue Ch. André, 69561, Saint Genis-Laval Cedex, France
[4] Department of Earth and Space Science, Chalmers University of Technology, Onsala Space Observatory, 43992, Onsala, Sweden
[5] Centro de Astrobiología (INTA-CSIC), Ctra de Torrejón a Ajalvir, km 4, 28850 Torrejń de Ardoz, Madrid, Spain
[6] Max-Planck-Institut für Extraterrestrische Physik, Giessenbachstraße 1, 85748 Garching, Germany
[7] Institute for Astronomy, The University of Edinburgh, Royal Observatory, Blackford Hill, Edinburgh EH9 3HJ, UK
[8] Institut d'Astrophysique Spatiale, CNRS, Université Paris-Sud, Bat. 120-121, F-91405 Orsay, France
[9] International Centre for Radio Astronomy Research, Curtin University, Perth WA 6845, Australia
[10] Jet Propulsion Laboratory, California Institute of Technology, Pasadena, CA 91109, USA
[11] Department of Physics and Astronomy, Johns Hopkins University, 3400 N. Charles St, Baltimore, MD, 21218, USA

October 14, 2015

ABSTRACT

We present a pilot study of the $z = 2.923$ radio galaxy MRC0943-242, where we for the first time combine information from ALMA and MUSE data cubes. Even with modest integration times, we disentangle an AGN and a starburst dominated set of components. These data reveal a highly complex morphology, as the AGN, starburst, and molecular gas components show up as widely separated sources in dust continuum, optical continuum and CO line emission observations. CO(1–0) and CO(8–7) line emission suggest that there is a molecular gas reservoir offset from both the dust and the optical continuum that is located ∼90 kpc from the AGN. The UV line emission has a complex structure in emission and absorption. The line emission is mostly due to *i*) a large scale ionisation cone energised by the AGN, *ii*) a Lyα emitting bridge of gas between the radio galaxy and a heavily star-forming set of components. Strangely, the ionisation cone has no Lyα emission. We find this is due to an optically thick layer of neutral gas with unity covering fraction spread out over a region of at least ∼ 100 kpc from the AGN. Other, less thick absorption components are associated with Lyα emitting gas within a few tens of kpc from the radio galaxy and are connected by a bridge of emission. We speculate that this linear structure of dust, Lyα and CO emission, and the redshifted absorption seen in the circum-nuclear region may represent an accretion flow feeding gas into this massive AGN host galaxy.

Key words. Galaxies: evolution – Galaxies: high redshift – Galaxies: active – Galaxies: ISM – Galaxies: halos

1. Introduction

Powerful high-z radio galaxies (HzRGs), defined as having $L_{3\,GHz} > 10^{26}\,\mathrm{W\,Hz^{-1}}$ and $z > 1$, are unique markers of the most active galaxies in the early Universe, showing signatures of both luminous AGN activity and vigorous starbursts. HzRGs are extremely luminous in both the mid-IR (Ogle et al. 2006; Seymour et al. 2007; De Breuck et al. 2010) and the sub-mm waveband (Archibald et al. 2001; Reuland et al. 2004; Drouart et al. 2014). This has been interpreted as evidence of high black hole accretion rates, combined with high star-formation rates (SFRs). HzRGs are some of the most massive galaxies known at any redshift, with $M > 10^{11}\,\mathrm{M_\odot}$ of stars (Seymour et al. 2007; De Breuck et al. 2010), confirming prior indications of their large masses from the tight correlation of the observed near-IR Hubble K-z diagram for these sources (Lilly & Longair 1984; Eales et al. 1997; De Breuck et al. 2002). In order to be so luminous, the black holes in these galaxies must be massive. Given that stellar bulge mass correlates with black hole mass (e.g. Tremaine et al. 2002), it is therefore no surprise that the most powerful radio galaxies reside in the most massive stellar hosts.

Disentangling the AGN and starburst components requires excellent sampling of the spectral energy distribution (SED). Seymour et al. (2012) illustrate the decomposition of the starburst and AGN components using 3.5 – 850 μm photometry in the $z = 2.16$ radio galaxy, PKS 1138-262, showing that both have roughly equal contributions to the IR luminosity. Disentangling the SED of HzRG is the main goal of our HErschel Radio Galaxy Evolution (HERGÉ) project (Drouart et al. 2014). The 71 HzRG targeted in the HERGÉ project are uniformly distributed across $1.0 < z < 5.2$ with a range of radio powers. *Spitzer, Herschel*, SCUBA and LABOCA data suggest that the sources targeted in the HERGÉ project have very high far-IR (FIR) luminosities ($\sim 10^{13}\,\mathrm{L_\odot}$, Drouart et al. 2014), but the data do not have high enough spatial resolution to pinpoint the AGN host galaxies as the source of the FIR emission. Resolution is important, as spec-

tral decomposition alone is probably insufficient to understand the evolutionary state of HzRGs.

Previous single sources studies of HzRGs have revealed that these systems have highly complicated morphologies, e.g. with line emission separated from the continuum emission. In several systems (e.g. 4C41.17 and 4C60.07, TXS0828+193, and B3 J2330+3927), most of the gas and dust emission originates from the companion rather than the AGN host galaxy, while others (e.g. MRC0114-211, MRC0156-252, and MRC2048-272) show no evidence for a companion (De Breuck et al. 2003, 2005; Ivison et al. 2008, 2012; Nesvadba et al. 2009; Emonts et al. 2014). These observations confirm that spectral decomposition alone is insufficient to understand the evolutionary state of HzRGs, sufficiently high spatial resolution to separate out individual emission components is also crucial.

The sub-arcsecond spatial resolution of ALMA will undoubtedly reveal a much more complex composition of AGN and starburst dominated sources than previously thought. To illustrate this point, we conducted a pilot study of MRC0943-242 at $z = 2.9$, where we combine - for the first time - sensitive ALMA 235 GHz and VLT/MUSE observations. This combination allows us to trace the spatially-resolved distributions of the ionisation state of the warm ionised medium (T$\sim 10^4$ K) through the UV emission and absorption lines (e.g. CIV), the warm neutral gas (T$\sim$ few $\times 10^3$ K) through Lyα absorption, and the dense and diffuse molecular gas as probed by the dust and high-J CO transitions. Through this combination it is possible to get a comprehensive picture of several important phases of gas in the interstellar medium and haloes of HzRGs.

MRC0943-242 is an ultra steep spectrum radio source with a spectral index of $\alpha = -1.5$ between 1.4 − 30 GHz and shows no evidence of a spectral curvature within this range (Carilli et al. 1997; Emonts et al. 2011). MRC0943-242 is located in a proto-cluster (with an over density of almost 5σ; Wylezalek et al. 2013) surrounded by many nearby companions detected in Lyα with known redshifts (Venemans et al. 2007) and a giant quiescent Lyα halo with a diameter of ≥ 100 kpc - extending far beyond the radio structure (Villar-Martín et al. 2003). A deep absorption trough in the Lyα emission line suggests the presence of a large amount of neutral gas (Röttgering et al. 1995). Based on a 1.5 Å-resolution spectrum Röttgering et al. (1995) conclude that the saturated absorption trough is due to a reservoir of neutral hydrogen (HI) situated within the HzRG it self. They determine a HI column density of $N_{\rm HI} = 10^{19}\,{\rm cm}^{-2}$ in the absorber. Using the same observational set-up, Binette et al. (2000) determine a HI column density similar to that of Röttgering et al. (1995) and a CIV column density of $N_{\rm CIV} = 10^{14.5\pm0.1}\,{\rm cm}^{-2}$. However based on Voigt-profile fittings to the absorption troughs in both the Lyα and CIV emission lines Binette et al. (2000) conclude that the reservoir of gas causing the absorption features is not situated within the HzRG, but rather due to a low metallicity ($Z = 0.01\,{\rm Z}_\odot$), low density gas in the outer halo at a redshift of $z = 2.29202 \pm 0.0002$. They propose that this gas is a remnant of gas expelled from the HzRG during the initial starburst. Though such a starburst is expected to enrich the expelled gas more than what is observed for MRC0943-242, Jarvis et al. (2003) still favored this scenario. Based on numerical simulations by Bekki (1998), which predict that the outer regions of galactic halos should be less metal-rich, Jarvis et al. (2003), as Binette et al. 2000, favored a picture where the shell lies in the halo to explain its the low metallicity. Furthermore, by comparing MRC0943-242 with another HzRG (MRC0200+015), they argue that the age of the system can have an influence on the metallicity of the shells. They conclude that the metallicities of absorption shells surrounding HzRG vary from galaxy to galaxy and from shell to shell. This implies that the shells must be enriched by a variety of processes. With UVES data with a spectral resolution of 25000-40000 Jarvis et al. (2003) identified three additional weaker absorbing components of different HI column densities.

In this paper, we present a study of MRC0943-242, where we for the first time combine relatively short ALMA submillimetre (submm) observations with MUSE optical observations. This ALMA-MUSE-pilot study reveals an even more complex morphology of MRC0943-242 than previously seen with star-formation taking place far outside the AGN host galaxy. In § 2 we present our ALMA submm and MUSE optical observations. The results of these observations are given in § 3 and are analysed and discussed in § 4. In § 5 we speculate as to the origin and role of the substructures and in § 6 we summarize our conclusion.

2. Observations

2.1. ALMA observations

The Atacama Large Milimeter/submilimeter Array (ALMA) cycle 1 observations in Band 6 were carried out on 2014 April 29 for 3 min on-source time with 36 working antennas. The four 1.875 GHz spectral windows were tuned to cover the frequency ranges 233.6 − 237.1 GHz and 248.6 − 252.3 GHz. We used the Common Astronomy Software Applications (CASA) and the supplied calibration script to calibrate the data, produce the data cube and moment 0 maps. The average $T_{\rm sys}$ was ∼80 K and the average precipitable water vapour 1.3 mm. The quasar J1037-2934 was used as bandpass calibrator and results in an astrometric accuracy of 4 mas. The UV coverage was sparse, but uniform over $\sim 400\,{\rm k}\lambda$. In order to search for CO(8–7) line emission at $\nu_{\rm rest} = 921.80$ GHz, which is within the frequency range at $z = 2.923$, we subtracted the continuum in the UV-plane by fitting a first-order polynomial to all four spectral windows, as no strong line emission is contaminating the continuum. As our data are limited by the signal-to-noise ratio (S/N), we use a natural weighting (robust parameter of 2). This results in a $0\farcs7 \times 0\farcs6$ beam with pa = 75° and an RMS of 0.1 mJy for the continuum. We binned the line data to 10 km/s which has an RMS of 1.7 mJy. As objects are detected up to 12″ from the phase centre, we applied a primary beam correction on all our maps and spectra.

2.2. MUSE observations

Multi Unit Spectroscopic Explorer (MUSE) (Bacon et al. 2010) observations were obtained on 2014 February 21, during the first commissioning run of the instrument (see Bacon et al. 2014) on VLT/UT4. This one hour observation taken under ∼ 1″ seeing was split into three 20 min exposures taken at 45, 135 and 225 degree position angle with a small dithering offset to minimise the effect of systematics. In order to observe the Lyα line of MRC0943-242 at 476.5 nm, we used the extended wavelength range mode (i.e. without second order blocking filter), resulting in a observed wavelength range of 460–935 nm). These data were taken specifically to compare MUSE observations with previous observations with other instruments of this well-studied source. Thus it serves as a pilot study for using MUSE to study HzRGs. All data were processed with the version 1.0 of the MUSE pipeline (Weilbacher et al. 2012) to produce a fully calibrated and sky subtracted data cube. Finally, the cube was cleaned for sky subtraction residuals with the Principal Component Analysis (PCA) based algorithm ZAP developed by Soto et

al (in prep.). To analyze the line emission and to remove a few artefacts in the data, we continuum subtracted the cubes around specific emission lines such as Lyα.

2.3. Previous Supporting Spitzer Observations

MRC0943-242 was observed among 68 other HzRG in the redshift range $1 < z < 5.2$ in a large *Spitzer* survey (Seymour et al. 2007). MRC0943-242 was observed with the Infrared Array Camera (IRAC), the Infrared Spectrograph (IRS) and the Multiband Imaging Photometer (MIPS) on *Spitzer*, which cover the wavelengths 3.6 μm, 4.5 μm, 5.8 μm, 8.0 μm, 16 μm, 24 μm, 70 μm and 160 μm (see Seymour et al. 2007 for details on the observations and reductions). At 3.6 and 4.5 μm, we use the deeper IRAC observations (Fig. 1) obtained as part of the Clusters Around Radio Loud AGN project (CARLA; Wylezalek et al. 2013).The IRAC and MIPS observations reveal that the continuum emission associated with the dust features in our ALMA data is very diffuse and faint (see section § 3.3 for more details). In support of the *Spitzer* data, we also examined the observations of MRC0943-242 from Keck and *HST/NICMOS* (van Breugel et al. 1998; Pentericci et al. 2001). We do not see any evidence at sub-arcsecond resolution of multiple components.

3. Results

Combining for the first time ALMA submm observations with MUSE optical observations reveals an even more complex morphology than seen previously: with multiple components where only the AGN dominated component is visible in all wavelengths. Figure 1 shows the IRAC 3.6 μm and 4.5 μm image, Lyα and HeII moment-0 maps in a colour image observed with MUSE and the 235 GHz map observed with ALMA. The Lyα moment-0 map shows a bright source at the position of the HzRG (hereafter Yggdrasil) and an additional component to the South-West (SW), connected by a bridge of Lyα emission (hereafter Bifrost). Yggdrasil is visible in all four images, while Bifrost splits up into three components in the 235 GHz observations (hereafter Freja, Thor and Odin). Thor is visible in the IRAC 3.6 μm and 4.5 μm images with an extension towards both Freja and Odin. A CO(8–7) emitting component (hereafter Loke) is located even further to the SW than Freja, Thor and Odin. The complex morphology is illustrated by the schematic overview in Fig. 1 and additionally shows the positions of the radio lobes, and the CO(8–7) emission at the position of Yggdrasil and Loke. We now discuss each of these phases in detail.

3.1. Surprising dust and molecular gas distribution

3.1.1. Dust continuum emission

Yggdrasil shows up in the ALMA submm observations as a weak dust continuum emission source at 235 GHz, with an extracted flux density over the region of 0.8 ± 0.2 mJy (see Table 4). However, the vast majority of the 235 GHz dust emission originates from three components (Freja, Thor and Odin) aligned along a "string" shifted $48 - 65$ kpc towards the SW relative to the position of Yggdrasil (see Fig 1). Table 4 lists their flux densities extracted using CASA.

Considering the number counts of > 0.5 mJy sources at 235 GHz of $\sim 2 \times 10^4$ deg^{-2} (Laurent et al. 2005), and the size of the area within the 8.″7 radius from Yggdrasil to Odin, we expect to find 0.37 sources with $F_{235\,GHz} > 0.5$ mJy. We detect four sources within this area; the probability that these four sources are unrelated is therefore 0.37^4, or 2%. The probability that these four sources are associated to MRC0943-242 is thus 98%.

3.1.2. Molecular emission lines

Searching the ALMA cube for molecular gas tracers, we find CO(8–7) emission at two different positions. One at the position of Yggdrasil and one $\sim$ 90 kpc SW of Yggdrasil. The 3.5σ CO(8–7) detection at the position of Yggdrasil (see Fig 2) is only shifted by $\sim$ +43 km/s from the HeII systemic redshift. Fitting a single Gaussian to this narrow velocity profile yields a FWHM of 47 ± 13 km/s, and a velocity integrated line flux of 0.33 ± 0.06 Jy km/s. The other 3.5σ CO(8–7) detection is located $\sim$ 90 kpc SW of Yggdrasil (Loke, see Fig. 1 and 2). Surprisingly, Loke is not detected in any dust continuum nor optical counter parts. Like the CO(8–7) line detected at the position of Yggdrasil, this CO(8–7) line is narrow with a FWHM of 53 ± 17 km/s, and only shifted by $\sim$ +16 km/s from the HeII systemic redshift (see Fig.4). The RMS of the CO(8–7) spectrum for Yggdrasil is 1.8 mJy and 2.1 mJy for Loke. This small difference is due to a combination of the primary beam correction (affecting only Loke) and continuum subtraction residuals (affecting only Yggdrasil, as no continuum is detected in Loke).

To verify the reality of the CO(8–7) emission, ensuring that these CO(8–7) lines are not rare but insignificant noise peaks in the cube, we create 13 moment-0 maps at different frequencies in the cube by collapsing a velocity ranges in the cube of 180 km/s. This corresponds to three times the average FWHM of two CO(8–7) lines and is the same velocity width as for the CO(8–7)-moment-0 map (see Fig. 2). From these, we select the brightest areas in each moment-0 map and extract the spectrum from the cube for each of these areas and ensure that there is no overlap between velocity regions. From this we find 81 unique peaks for which we extract over the full 233.5 – 236.5 GHz frequency range. We fit a Gaussian profile to the brightest peak in each spectrum and determine the S/N in each spectrum. Only two spectra show a peak of intensity with a S/N of $\sim$ 3 and a FWHM of $\sim$ 70 km/s which could resemble a real line. The chance of detecting a line such as Loke within 27±6 km/s from Yggdrasil within our 4000 km/s bandwidth is $27/4000 = 0.67\%$. In addition, the probability of finding a $\sim$ 50 km/s wide line like Yggdrasil and Loke is $50/4000 = 1.25\%$. The combined probability of finding the observed CO(8–7) configuration in Loke and Yggdrasil is therefore only 0.84%.

Searching the archival Australian Telescope Compact Array (ATCA) data for Yggdrasil (see Emonts et al. 2011 for more details about the data reduction and data characteristics) by reshifting the velocities to the redshift ($z = 2.92296 \pm 0.00001$ see § 3.2) used for this work, we find tentative CO(1–0) line emission at a 2.8σ level at the position of Loke (see Fig. 2), consistent with the existence of a large molecular gas reservoir. The tentative detection of CO(1–0) emission and the CO(8–7) to CO(1–0) line flux ratio of $\sim$ 0.03 would imply the presence of a low excitation molecular gas reservoir. No CO(1–0) emission was found at the position of Yggdrasil (see Fig. 2). This agrees with the expectation that we should find more highly excited gas near a powerful radio-loud AGN (e.g. Weiß et al. 2007)

Unfortunately the ATCA observations are limited by the large beam and low S/N, and it is therefore not possible to determine whether or not CO(1–0) emission originates from the dust continuum sources, a free molecular gas component in the halo or both. In an attempt to explore if an extended CO(8–7) component is present, we applied a larger beam to the ALMA 235 GHz data. Unfortunately, tapering the ALMA 235 GHz data and con-

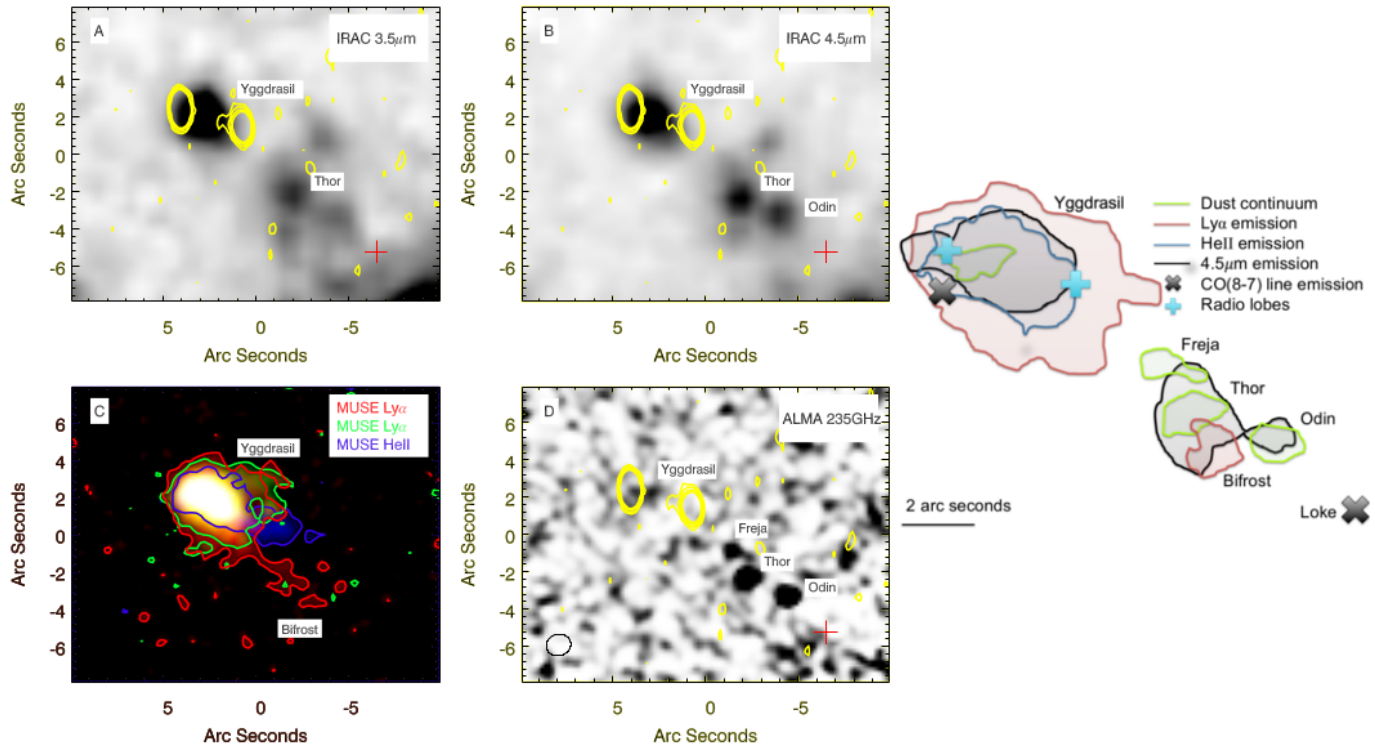

Fig. 1. Overview of the IRAC (3.6 μm and 4.5 μm), MUSE (Lyα and HeII) and ALMA (235 GHz) maps. *Panel A and B*: The IRAC 3.6 μm and 4.5 μm images showing both Yggdrasil and Thor. Both IRAC images have a spatial sampling of 0.61″/pixel. *Panel C*: A red (Lyα), green (Lyα) and blue (HeII) image composed of moment-0 maps of the MUSE cube, which have an spatial sampling of 0.2″/pixel. The red Lyα moment-0 is summed over $\lambda_{\rm obs}$ = 4768.8 – 4776.2 Å(see red bar in panel A of Fig. 5), the green Lyα moment-0 is summed over $\lambda_{\rm obs}$ = 4754.3 – 4758.8 Å (see green bar in panel A of Fig. 5) and the blue HeII moment-0 map is summed over $\lambda_{\rm obs}$ = 6422.5 – 6430.0 Å. The red Lyα reveals a bridge of emission connecting Yggdrasil and Bifrost (see § 3), while the green Lyα emission shows extended emission to the west. The Blue HeII shows an extended tail of HeII emission towards the WSW, which is not seen in Lyα emission (see § 3.2). *Panel D*: The ALMA dust continuum map reveals weak dust emission at the position of the AGN, but strong dust emission in three aligned components 48-65 kpc SW of the AGN. The mm continuum flux density of all four continuum sources are extracted with apertures of; Yggdrasil: 2.6″ × 1.7″, Freja: 1.8″ × 1″, Thor; 1.9″ × 1.5″ and Odin: 1.2″ × 1.4″. *Far right*: Schematic overview of the multi-wavelength components detected in MRC0943-242. VLA 4.5 GHz radio observations have been overlaid in yellow contours in Panel A, B and D. The plotted contour levels are for -3σ, $2\times3\sigma$, $3\sqrt{2}\times3\sigma$, $5\sqrt{2}\times3\sigma$, which is the same for all VLA contour levels through out the paper. The position of Loke is marked with a red cross in Panel A, B and D.

volving them with a beam comparable to that of ATCA did not produce useful results, as our shallow ALMA observation do not contain sufficient short baselines. We plan JVLA CO(1–0) and ALMA [CI] observations at arc-second spatial resolution to pinpoint the exact location and determine the characteristics of the molecular gas reservoir.

No CO(8–7) line emission is observed at the positions of Freja, Thor and Odin. We therefore take the 3σ upper limit of the line emission at these positions to be 3 times the RMS of the spectra extracted with the same region sizes as for the continuum emission (see Table 1).

3.2. Ionised gas

The MUSE spectrum of Yggdrasil (Fig. 3) detects a rich variety of ionised gas tracers. Overall, our spectrum is consistent with the Keck spectrum of Vernet et al. (2001), but now provides full spatial information over the large field (1′×1′) of view of MUSE. Table 1 lists the velocity and integrated fluxes for the nine emission lines detected at the position of Yggdrasil. The flux is determined by integrating the spectral line profile within 3σ of the noise. For our analysis, we adopt the redshift of HeII integrated over the peak of the continuum emission as the systemic velocity, as it is the brightest non-resonant line in our spectra. The HeII emission line is best fitted by a Lorentzian profile, with a centre corresponding to a redshift of 2.92296 ± 0.00001 and a FWHM of 862 ± 30 km/s. The flux within 3σ is given in Table 1. The other high ionisation lines have profiles and redshifts similar to that of HeII (Table 1) and Fig. 4.

The Lyα (λ1215.7 Å) line is by far the brightest and most extended emission line in the MUSE data cube. It peaks at the position of the AGN, but extends out to 80 kpc (see bottom panel of Fig. 5). Such extended Lyα haloes have been detected in several other HzRGs (e.g. van Ojik et al. 1996; Reuland et al. 2003; Swinbank et al. 2015). The Lyα halo in MRC0943-242 shows a linear filament, Bifrost, connecting Yggdrasil with the two brightest dust continuum components (Thor and Odin), strongly suggesting that they are physically connected (see Fig 5). The peak intensity of Bifrost is ∼ 18 times fainter than that for the Lyα detection of Yggdrasil (see panel A and D of Fig. 5).

The Lyα emission on the nucleus exhibits four absorption features in our data. We denote these absorption features as 1, 2, 3 and 4 where the bluest feature is 1, middle are 2 and 3, and the reddest absorption feature 4 (in accordance with the labelling used by Jarvis et al. 2003, see panel A of Fig. 5). Furthermore, component 2 is related to the strong CIV absorption observed against the nucleus (Binette et al. 2000). By centering the Lyα velocity profile at the fitted central velocity of HeII we

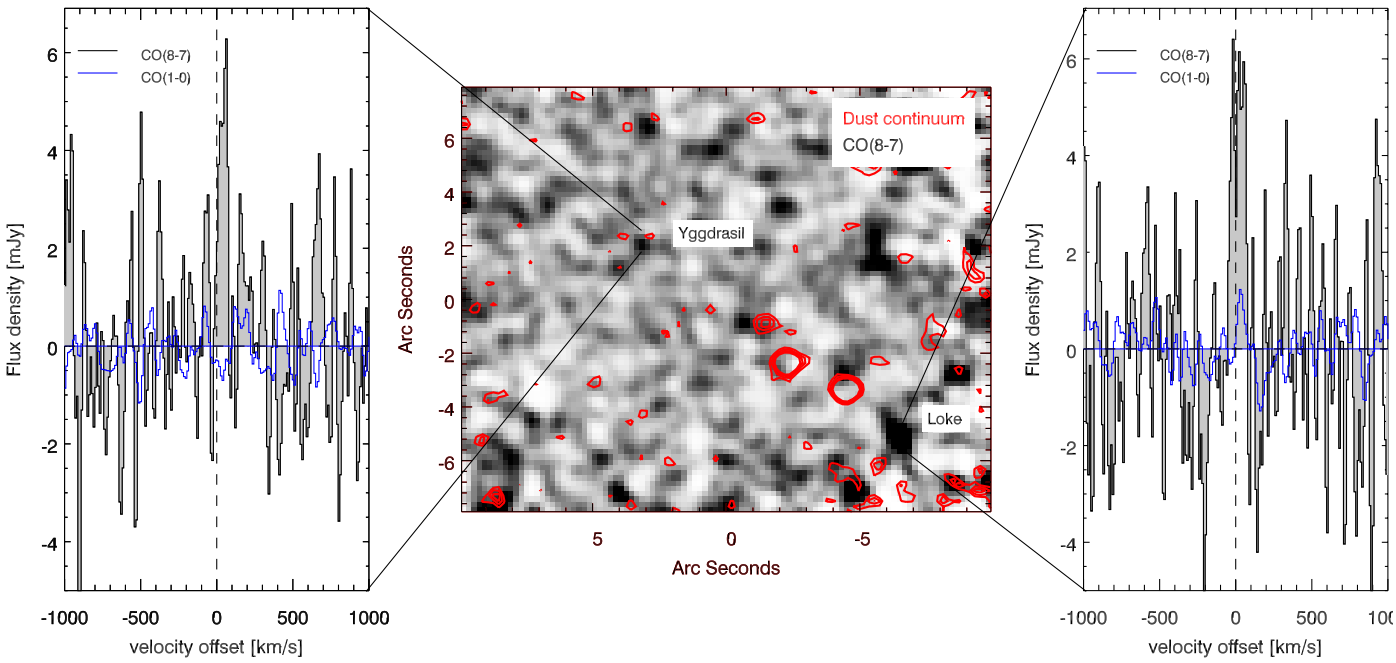

Fig. 2. The ALMA cube shows CO(8–7) emission at two positions in the data cube: at the location of Yggdrasil and to the SW in an isolated component: Loke. *Middle panel:* The grey scale image of the CO(8–7) emission overlaid with the ALMA dust continuum contours. Note the increase in noise towards the edges due to the primary beam correction. *Left and Right:* The CO(8–7) velocity profiles for both Yggdrasil (left) and Loke (rigth). Surprisingly the CO(8–7) lines only have a small offset from the HeII systemic redshift. The spectra are extracted from a beam-sized area at the position of the emission, and have RMSs of 1.5 mJy and 1.0 mJy respectively. Both detections are unresolved at the S/N of our data.

find that the bottom of the absorption trough is at a redshift off $z_{\rm abs} = 2.91864 \pm 0.00002$. By fitting a Voigt-profile to the absorption trough, we estimate a column density of the neutral gas for component 2 of $N_{\rm HI} = 1.3 \cdot 10^{19}$ cm^{-2} and a Doppler width of 64 km/s (see Table 2) which are comparable to the values determined by Binette et al. 2000. We note that because the line is saturated, this estimate is very uncertain and likely a lower limit to the true value. For components 1, 3 and 4, we find good agreement with the values in Jarvis et al. (2003) for the column densities and velocities.

We observe two absorption troughs in the CIV emission line; Voigt profile fitting to the two features reveals that they are caused by gas on the line of sight at redshift $z_{\rm abs} = 2.91940 \pm 0.00007$ and 2.91945 ± 0.000061 and column densities of $N_{\rm CIV} = 3.4{\cdot}10^{14}$ cm^{-2} and $= 6.9{\cdot}10^{14}$ cm^{-2}, higher than $3.2{\cdot}10^{14}$ cm^{-2} found by Binette et al. 2000.

Stepping through the cube towards increasing wavelengths reveals the complexity of the emission in the MRC0943-242 system (see Fig. 5, 6 and 7):

• $\lambda_{\rm obs} \sim 4732 - 4747$ **Å:** Considering the Lyα emission line profile at Yggdrasil (see panel A of Fig. 5); the emission furthest to the blue side of the line profile is spatially centred around the radio source and approximately within the region containing the radio emission (see also panel A Fig. 6).

• $\lambda_{\rm obs} \sim 4747 - 4754$ **Å:** As we move towards the red, over the wavelength range of absorption feature 1, we see strong nuclear emission.

• $\lambda_{\rm obs} \sim 4754 - 4759$ **Å:** Moving further to the red between absorption features 1 and 2, we observe a closed region of bubble-like emission reaching $\sim$ 20 kpc out, surrounding the western radio lobe (see panel B of Fig. 6). The absorption components 1 and 2 are visible against this emission across the region of Yggdrasil (see panel A-C of Fig. 5).

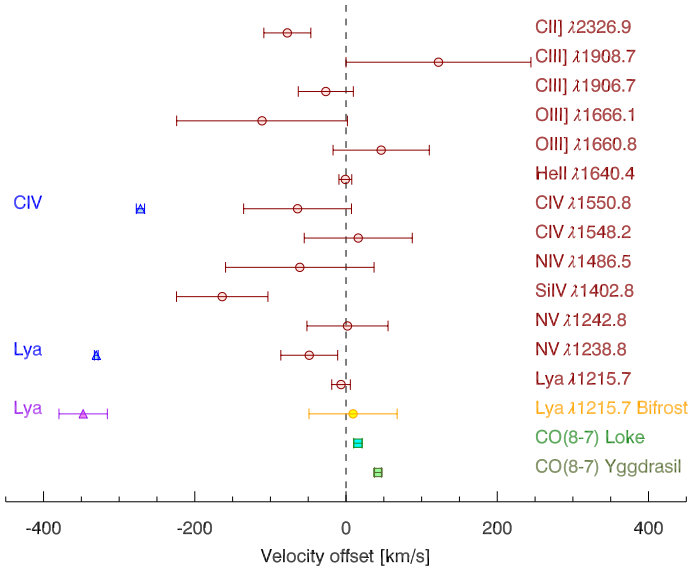

Fig. 4. The offset of the emission line and absorption features centers from the HeII systemic redshift. Red points are emission lines observed for Yggdrasil. Yellow is the Lyα emission line for Bifrost. Green is the CO(8–7) emission lines for Yggdrasil and Loke. Blue and purple are the center of the absorption feature 2. The emitting components are distributed within ±200 km/s of the systemic velocity, while the absorbers are all blue shifted by ~350 km/s.

• $\lambda_{\rm obs} \sim 4759 - 4769$ **Å:** As we step further to the red, through the wavelength range of absorption feature 2, the Lyα emission becomes fainter – down to our surface brightness detection limits. We note that this is in agreement with the Lyα profiles of all the extended emission – when we have sufficient surface brightness to have detectable line emission, we see absorption compo-

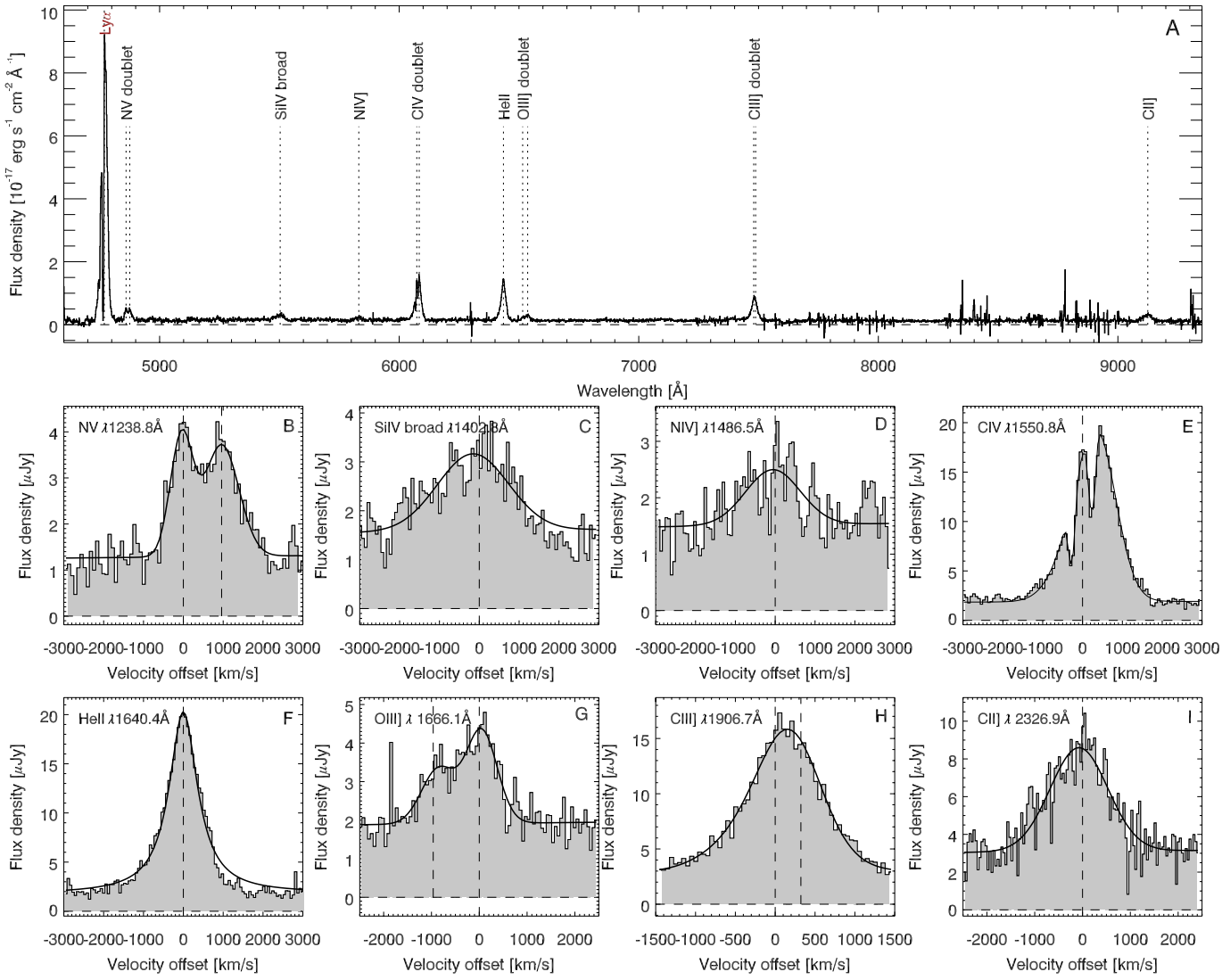

Fig. 3. The top panel shows the full MUSE spectrum for Yggdrasil. All detected lines (other than Lyα) are indicated with a black dotted lines, and the velocity profiles are shown in Panel B-I. The velocity profiles for NV, SiIV, NIV], CIV, HeII, OIII],CIII], and CII] assume HeII as the systemic redshift. The CIV emission line shows absorption troughs like those of the Lyα emission line.

Line	$N_{\rm HI}$ cm^{-2}	b km/s	$z_{\rm abs}$
Yggdrasil			
Lyα absorber 1	$5.0 \cdot 10^{13}$	84	2.90689 ± 0.00032
Lyα absorber 2	$1.3 \cdot 10^{19}$	64	2.91864 ± 0.00002
Lyα absorber 3	$3.7 \cdot 10^{13}$	140	2.92641 ± 0.00023
Lyα absorber 4	$1.7 \cdot 10^{13}$	33	2.93254 ± 0.00007
CIV absorber 2	$3.4 \cdot 10^{14}$	94	2.91940 ± 0.00007
	$6.9 \cdot 10^{14}$	100	2.91945 ± 0.00006
Bifrost			
Lyα absorber 2	$7 \cdot 10^{18}$	—	2.91841 ± 0.00045

Table 2. Parameters determined by fitting a Voigt profiles to the absorption troughs. Fits are performed on the absorption troughs in the Lyα line observed for both Yggdrasil and in-between Odin and Thor. The CIV line has been fitted with two Voigt profiles with the same fitting parameters.

nent 2 which has zero intensity in the line core. This includes the Lyα emission from Bifrost (see panel D in Fig. 5) and the CIV emission from Yggdrasil. The absorption component 2 in Bifrost is at a redshift of $z_{\rm abs} = 2.91841 \pm 0.00045$, consistent with that in Yggdrasil (see panel D of Fig 5). This suggests that the absorption feature in the spectrum of Bifrost is due to absorption component 2, meaning that absorber 2 has an extent of at least 65 kpc from Yggdrasil. The data suggest a lower column density of absorber 2 in Bifrost of $N_{\rm HI} \sim 7 \cdot 10^{18}$ cm^{-2}. We warn that this $N_{\rm HI}$ is particularly uncertain due to the low S/N of the data, and the degeneracy between $N_{\rm HI}$ and the b-parameter. Deeper and higher resolution data are required to trace column density variations across the system. We also note that in this wavelength range, we observe high ionisation emission lines of HeII, CIV, and CIII] from gas extending over 7″ or ∼ 60 kpc to the west (see panel F, the green contours of the central panel of in Fig. 5 and the CIV and HeII moment-0 maps in panel A and B of Fig. 7). Fainter, less extended emission is also observed to the east of the nucleus. Deeper data will be needed to determine the exact distribution of absorption component 2; however, since the line core is black throughout the extend of the cube, we can conclude that it is extended with a unity covering factor.

MUSE				
Line	$\lambda_{\rm rest}$ Å	$\lambda_{\rm obs}$ Å	Line flux 10^{-16} erg/cm^{-2}/s	FWHM km/s
Yggdrasil				
Lyα	1215.7	4768.9 ± 0.2	26.60 ± 0.25	1592 ± 44
NV	1238.8, 1242.8	4859.1 ± 0.6, 4875.5 ± 0.9	0.90 ± 0.04	1803 ± 174
SiIV	1402.8	5500.1 ± 1.1	0.60 ± 0.04	2493 ± 214
NIV]	1486.5	5830.3 ± 1.9	0.27 ± 0.04	1764 ± 370
CIV	1548.2, 1550.8	6073.9 ± 1.5, 6072.2 ± 1.4	4.34 ± 0.06	1410 ± 188
HeII	1640.4	6435.2 ± 0.2	3.04 ± 0.05	862 ± 30
OIII]	1660.8, 1666.1	6516.3 ± 1.4, 6533.8 ± 2.5	0.50 ± 0.03	1492 ± 292
CIII]	1906.7, 1908.7	7479.2 ± 0.9, 7490.9 ± 3.1	2.00 ± 0.06	1734 ± 124
CII]	2326.0	9122.4 ± 1.0	0.90 ± 0.04	1606 ± 118
Bifrost				
Lyα	1215.7	4769.2 ± 1.1	0.65 ± 0.06	1018 ± 205
ALMA				
Line	$\nu_{\rm rest}$ GHz	$\nu_{\rm obs}$ GHz	$S\,dV$ Jy km/s	FWHM km/s
Yggdrasil				
CO(8–7)	921.8	234.94 ± 0.1	0.33 ± 0.07	43 ± 13
Loke				
CO(1–0)	115.3	—	< 0.08	27 ± 16
CO(8–7)	921.8	234.96 ± 0.1	0.54 ± 0.10	57 ± 17
Freja, Thor and Odin				
CO(8–7)	921.8	—	< 0.13	—
CO(8–7)	921.8	—	< 0.18	—
CO(8–7)	921.8	—	< 0.16	—

Table 1. Velocity integrated fluxes and FWHM of the resonance , fine-structure, and molecular lines for Yggdrasil, in-between Odin and Thor and Loke. The ATCA observations have a beam size $11.5'' \times 9.0''$ and PA 87.5°. The 3σ upper limits on the CO(8–7) line emission for Freja, Thor and Odin are given assuming a FWHM of 50 km/s, i.e. similar to the CO(8–7) lines for Yggdrasil and Loke.

• $\lambda_{\rm obs} \sim 4769 - 4776$ **Å:** At wavelengths to the red of absorption feature 2, and containing the absorption feature 3 (see red contours of Fig. 5 and panel C in Fig. 6), we observe the emission from Bifrost. Where the Lyα emission is sufficiently bright, we see absorption component 3 superposed on the line emission (see panel A-C of Fig. 5).

• $\lambda_{\rm obs} \sim 4779 - 4794$ **Å:** Further to the red - at longer wavelengths than the range of absorption feature 3, component 4 shows up as a small trough (see panel A-C of Fig. 5 and panel D of Fig. 6) before we again start to see circum-nuclear emission all contained within the radius encompassing the radio lobes.

• $\lambda_{\rm obs} \sim 6025-6125$ and $6422-6430$ **Å:** Moving to wavelengths of the CIV and HeII emission, we do not have sufficient S/N to split these lines into velocity channels like for Lyα. Instead, we present line maps of the central parts of these lines in panels A and B of Fig. 7. Both lines display a similar morphology, which is also seen (albeit at lower S/N) in CIII] (panel C of Fig. 7). We detect a tail of CIV and HeII emission to the WSW (panels A and B of Fig. 7); however this tail is not spatially aligned with the Lyα bridge (Bifrost) connecting Yggdrasil with Freja, Thor and Odin. Interestingly, the CIV and HeII tail is not seen in Lyα (see the blue contours of the middle panel and panel E of Fig. 5). Fitting a Lorentz profile to this HeII emission line as well yields a redshift of $z = 2.916$ which is consistent with the emission being at the same velocity offset as absorption component 2. This suggest that this CIV and HeII emitting gas is also seen in Lyα, but that this is absorbed completely by component 2.

The large wavelength coverage of MUSE allows us to detect other fine structure lines (see panel B-I of Fig. 3). The three doublets NV, OIII] and CIII] are well detected at a $\geq 6\sigma$ level. The NV doublet is spatially resolved and reveals two spectral lines of similar intensity. The OIII] doublet is blended, but there is some indications of the doublet structure with the λ1660.8 Å line being a shoulder in the blue side of the OIII] λ1666.1 Å line. We also detect a broad SiIV component, a weak NIV] line at a 2.3σ level, and a CII] line at a 5.5σ level at the edge of the band. The CII] emission line is a blend of multiple lines, which explains why the line peaks on the red side of λ2326 Å. Table 1 lists the line parameters for these fine structure lines over the circum-nuclear region (see Fig. 3).

All the emission from NV, SiIV, NIV], OIII], and CII] lies within the region emcompassed by the radio lobes. The CII] emission is a particularly spectacular example as it delineates both the extension and direction of the radio jet and lobes (see panel D of Fig. 7).

3.3. Stellar mass

The wavelengths covered by *Spitzer* probe the rest-frame near- and mid-IR part of the spectrum, which is believed to be the best tracer of the stellar-mass with almost no contributions from the thermal emission from the AGN (Seymour et al. 2007). Yggdrasil has a well sampled SED with detections at 3.6 μm, 4.5 μm, 8.0 μm 16 μm, 24 μm, and upper limits for 5.8 μm, 70 μm and 160 μm. Seymour et al. 2007 and De Breuck et al. 2010 fit a toy model to these points, composed of four components: an elliptical galaxy composite stellar population (CSP) and three blackbody (BB) components with temperatures of 60 K, 250 K and between 500-1500 K (for more details see Seymour et al.

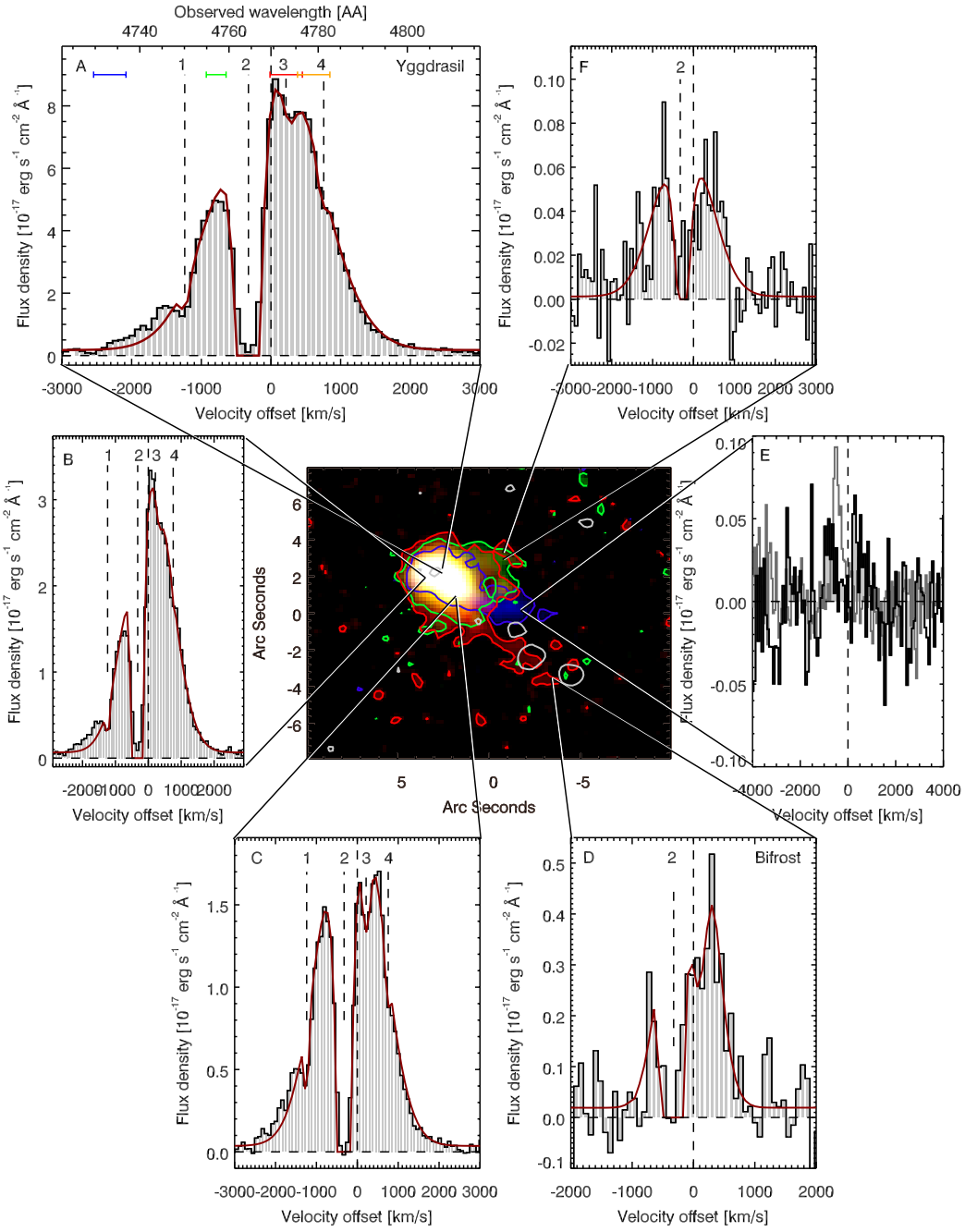

Fig. 5. Overview of emission and absorption components at different positions around MRC0943-242. *Middle Panel:* Composite Red-Green-Blue image of Lyα and HeII emission (see caption of Fig. 1 for more details) with the ALMA 235 GHz contours overlaid in grey. *Panel A:* The Lyα line profile of the full area of Yggdrasil (elliptical aperture of 1.3″ × 0.7″), showing all four absorption components. Component 2 is the most prominent and goes to zero intensity at its center. The spectrum has an RMS of $0.3{\times}10^{-17}$ erg s^{-1} cm^{-2} Å^{-1}. The blue, green, red and orange bars above the spectrum shows the range in wavelength the channelmaps in Fig. 6 have been summed over. The blue correspond to panel A, green to panel B, red to panel C and orange to panel C in Fig. 6. *Panel B and C:* The Lyα profiles of two areas near the nucleus (circular 0.5″ apertures) and have RMS of $0.1{\times}10^{-17}$ erg s^{-1} cm^{-2} Å^{-1}. These profiles likewise show signs of all four absorption components. *Panel D:* The Lyα profile of Bifrost (circular 1.2″aperture and RMS of $0.1{\times}10^{-17}$ erg s^{-1}) showing sign of absorption component 2. *Panel E:* Spectrum extracted at the HeII emitting tail (0.7″ aperture), showing no sign of Lyα emission and an RMS of $0.02{\times}10^{-17}$ erg s^{-1} cm^{-2} Å^{-1}. The HeII lines is over-plotted in grey. *Panel F:* The Lyα profile of the western extended Lyα emitting gas (0.4″ aperture). All Lyα velocity profiles have been fitted with Voigt profiles superimposed on a Gaussian profile. These fits are shown as the red curves over plotted on the spectra.

2007 and De Breuck et al. 2010). This SED fitting results in an H-band stellar luminosity of $L_H^{\rm stellar} = 2.5 \cdot 10^{11}$ L$_\odot$, which is converted to a stellar mass of $1.7 \cdot 10^{11}$ M$_\odot$ by assuming a dust-free, passively evolving elliptical galaxy which started its formation at $z = 10$ with no recent episodes of star-formation. The SED allows for a good decomposition of the stellar and hot-dust dominated components, so the derived stellar mass is expected to be reliable (see Seymour et al. 2007, for a more detailed discussion on the uncertainties).

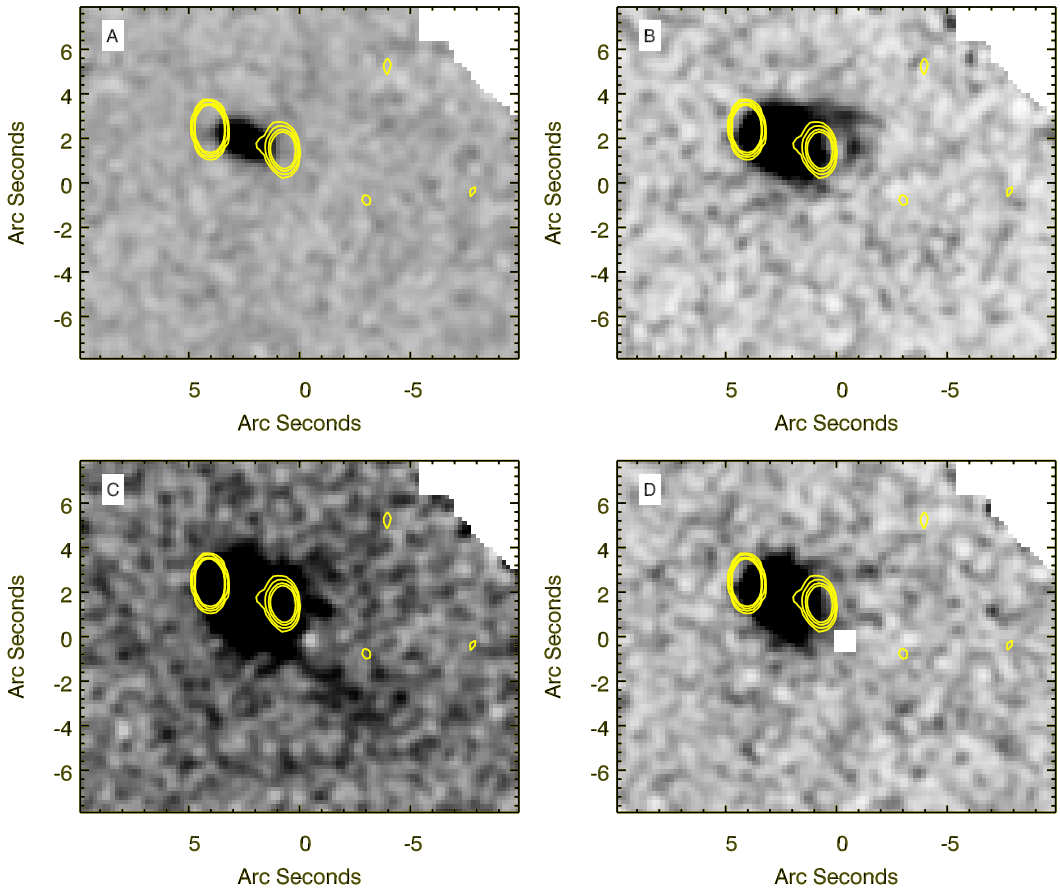

Fig. 6. Lyα Moment-0 maps summed over the wavelength ranges illustrated with the coloured bars in panel A of Fig. 5: *Panel A:* sum over the blue bar ($\lambda_{\rm obs}$ = 4732.5 – 4747.5). *Panel B:* sum over the green bar ($\lambda_{\rm obs}$ = 4754.3 – 4758.8). *Panel C:* sum over the red bar ($\lambda_{\rm obs}$ = 4768.8 – 4776.2). *Panel D:* sum over the orange bar ($\lambda_{\rm obs}$ = 4778.8 – 4793.8)

Instrument	wavelength	$S_{\rm Yggdrasil}$	$S_{\rm Thor}$	$S_{\rm Loke}$
	μm	μJy	μJy	μJy
IRAC 1	3.6	21.9	9.02	<2.10
IRAC 2	4.5	36.1	21.0	<1.32
IRAC 3	5.8	—	—	—
IRAC 4	8.0	30.2	< 21.4	—
MIPS	24	468 ± 40	180 ± 40	—

Table 3. The photometric IRAC and MIPS points for Yggdrasil, Thor and Loke after de-blending. Thor is not detected in the IRAC 3 image, however the flux at the position is influenced by an image artefact from a nearby star in the field. Extracting even an upper limit at this position is therefore not possible. Loke is not detected in any of the IRAC images; we quote the 3σ upper limits (Wylezalek et al. 2013).

Component	Position		$S_{235\,\rm GHz}$
	RA	dec	mJy
Yggdrasil	09:45:32.769	-24.28.49.29	0.8 ± 0.2
Odin	09:45:32.222	-24.28.55.06	2.0 ± 1.0
Thor	09:45:32.386	-24.28.54.05	1.9 ± 0.8
Freja	09:45:32.445	-24.28.52.55	0.6 ± 0.3
Loke	09:45:32.072	-24.28.56.94	< 0.3

Table 4. Positions and 235 GHz fluxes for all components of MRC0943-242. As no dust continuum is observed for the position of Loke we infer a 3σ upper limit of the 235 GHz of three times the rms. The uncertainty includes the 15% flux calibration error.

Component	$L_{\rm IR}$	perc.
	[10^{12} $L_\odot$]	
Total (Yggdrasil+Freja+Thor+Odin)	17.2	100
Freja+Thor+Odin (SB)	8.4	49
Yggdrasil (AGN)	7.5	43
Yggdrasil (SB)	1.3	8

Table 5. Infrared luminosities of each component, determined from our SED presented in Fig 8.

Examining the IRAC 3.6 μm and 4.5 μm image again, now with the knowledge of the presence of Freja, Thor and Odin, we find stellar emission at the position of Thor, with an extension towards Freja and Odin (see Fig. 1 top left and Table 3). Also for Thor are the stellar and hot-dust emission well separated in the SED. We scale the stellar mass found for Yggdrasil, to the emission seen in the IRAC 4.5 μm map (Table 6), yielding a stellar mass of 1.0×10^{11} $M_\odot$. For Loke, we accordingly derive an upper limit to the stellar mass of $\lesssim 6.2 \times 10^9$ $M_\odot$.

3.4. Disentangling the SED

Yggdrasil has a well-sampled SED with IRAC, MIPS, SPIRE (250 μm, 350 μm and 500 μm) and PACS (24 μm, 100 μm and 160 μm) from previous studies (De Breuck et al. 2010; Drouart

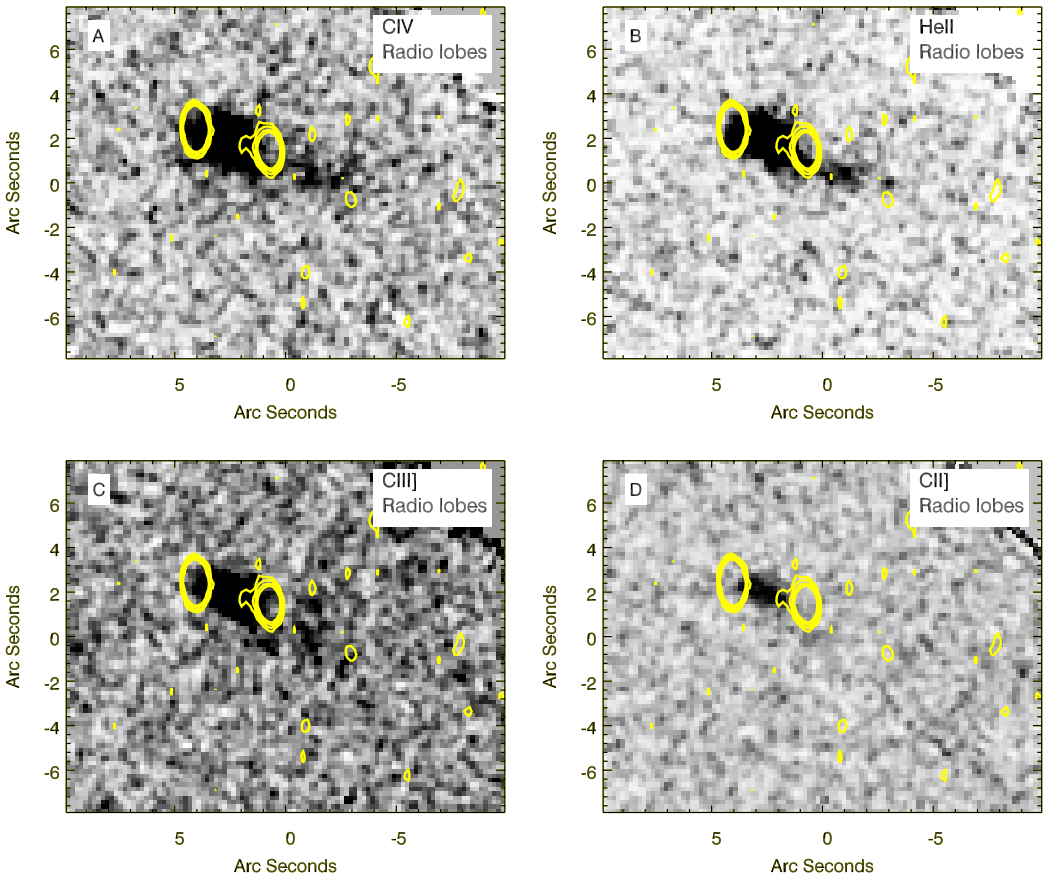

Fig. 7. Continuum subtracted moment-0 maps of the CIV, HeII, CIII] and CII] emission lines. The continuum is determined from the nearby line free channels for each line. *Panel A:* sum over the CIV emission line for the wavelength range λ_{obs} = 6050 – 6090 Å. *Panel B:* sum over the HeII emission line for the wavelength range λ_{obs} = 6422 – 6430 Å and is the same image as the blue colour of the middle panel of Fig. 5. *Panel C:* sum over the CIII] emission line for the wavelength range λ_{obs} = 7455 – 7485 Å. *Panel D:* sum over the CII] emission line for the wavelength range λ_{obs} = 9071 – 9171 Å. Over-plotted with yellow contours in all panels is the VLA radio map, as a reference.

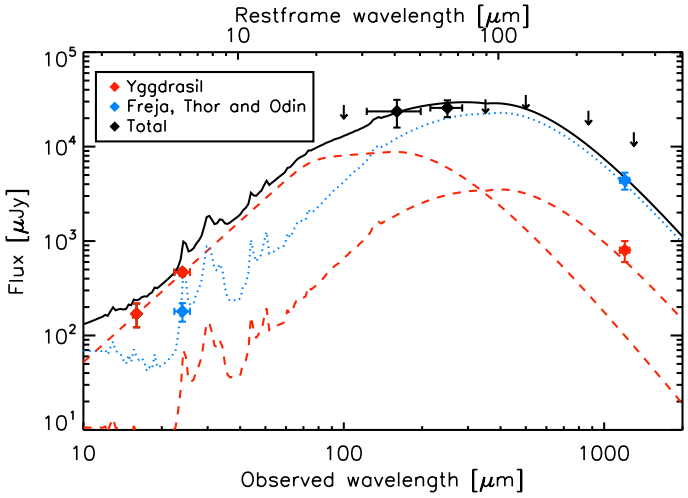

Fig. 8. The spectral energy distribution of MRC0943-242. The spatial resolution of the ALMA data allows us to disentangle the SED in the AGN heated component (red curve) and star formation heated component (blue curve). The sum of these two components is illustrated by the black curve.

et al. 2014). The PACS 160 μm image (see Appendix C of Drouart et al. 2014) reveals an elongated source, spanning from the position of Yggdrasil towards Freja, Thor and Odin. Likewise, when returning to the IRAC 3.6 μm and 4.5 μm images (see panel A and B of Fig. 1), multiple components show up corresponding to Yggdrasil and Thor (see §3.3). While these sources can be separated in the *Spitzer* data, they are blended in the *Herschel* data. However, the high spatial resolution and sensitivity of the ALMA data allows us to disentangle the AGN and star formation heated components in the SED at 235 GHz. We conclude that the star-formation, as probed by the dust emission, is taking place at a distance of 48-65 kpc from the AGN in three smaller aligned components (Freja, Thor and Odin). Table 3 lists the de-blended MIPS and IRAC photometry points.

Relying on the method of Drouart et al. 2014 by fitting an SED with AGN and starburst components, we now go further, and use the sub-arcsec resolution provided by the new dust continuum image to further disentangle the relative contribution of AGN and star formation *spatially*. Figure 8 shows the composite SED of the system, the three components being two spatially distinct positions with *i*) Yggdrasil *ii*) and Freja, Thor and Odin photometry as red and blue points respectively. The unresolved far-IR *Herschel* detections and upper limits are shown as black points. It is important to note that each component is fitted individually, and that the black points are not used in the fit. However, the total SED and unresolved data (in black) provide a strong constraint on the total integrated flux from all components; all solutions where the sum is inconsistent with the *Her-*

schel photometry are excluded. In practice, the starburst component in Freja, Thor and Odin is well constrained (blue dotted line in Fig. 8). However, the AGN component cannot simultaneously fit both the *Spitzer* and ALMA photometry without exceeding the *Herschel* photometry. We are therefore forced to add an additional starburst component to fit the Yggdrasil ALMA point. However, with only a single point, the starburst luminosity is only loosely constrained.

We clearly see from the SED fitting that Thor is star-formation dominated, with the MIPS 24 μm and 235 GHz reproduced by the starburst model from DecompIR (Mullaney et al. 2011). Yggdrasil represents a composite of emission from an AGN and star formation as reported earlier (Drouart et al. 2014). However, the relative contribution to the IR luminosity from the AGN and the star formation is different; favoring the AGN as the main contributor. In fact, the AGN emits ∼40% of the IR luminosity of the entire system ($L^{\rm IR}_{\rm total} = 1.7 \times 10^{13}\,{\rm L}_{\odot}$), the remaining ∼ 60% is star-formation split between *i*) Yggdrasil and *ii*) Freja, Thor and Odin at ∼10% and ∼50% levels (Table 3.4). According to the Kennicutt (1998) relation, Yggdrasil and Freja, Thor and Odin have SFR of ∼ 200 and ∼ 1400 $\rm M_{\odot}\,yr^{-1}$, respectively. Which, in turn, corresponds to a sSFR of $\sim 10^{-9}$ and $10^{-8}\,\rm yr^{-1}$.

4. Discussion

The wealth of information provided by the MUSE and ALMA data, even with rather modest integration times for both sets of data, paints a complicated picture from the warm ionised gas to the cold molecular gas and dust. We now discuss how the mass is distributed in each component and what the relationship between the components is.

4.1. The nature of the gas and dust

The MRC0943-242 system has a complex distribution of the ionised and neutral gas. The high ionisation lines are distributed mainly around the nucleus and are confined within the radio lobes. The exception to this is the extended HeII, CIV, and CIII] emission which is most extended to the west – beyond the western radio lobe (see panel A-C of Fig. 7). The fact that metals are detected within this part of the halo suggests the gas is not pristine, while the high ionisation state of the gas is consistent with photoionisation by the AGN, indicating that there is a cone of ionisation along the direction of the radio jet but extending well beyond the radio lobes. The lack of very extended Lyα emission in the outer region of the ionisation cone is most likely caused by HI gas distributed over large scales absorbing the emission (absorption component 2). The inner regions of the ionisation cone, i.e. the region that lies within or just beyond the radio lobes, shows significant Lyα emission (and also absorption from component 2). Resonance scattering shifts the frequency of the Lyα photons and allow them to 'leak' out on both sides of the absorption feature and broaden the line. In fact, throughout the region of Yggdrasil, we see all absorption components either in all places (as for components 1, 2 and 3) or in particular regions (as for component 4). Since the absorption features are only rarely reaching zero intensity in their cores, the neutral gas responsible for absorption systems 1, 3, and 4 are mixed with Lyα line emitting regions (although some of it overlies the Lyα emission). Absorption component 2 must cover the full Lyα emitting region, including that out to ∼60 kpc, which is the projected distance to Bifrost. Since this absorption contains no flux in the line core (it is dark), the absorber must have unity covering factor and be optically thick. This being the case, our estimate of the HI column density is a lower limit.

This situation is somewhat akin to the large extended Lyα absorber on the line of sight to the HzRG TN J1338-1942 at $z = 4.1$ (Swinbank et al. 2015). In this case the neutral gas reservoir extends at least 150 kpc away from the core of the HzRG. To detect this extended emission, Swinbank et al. (2015) obtained a much deeper integration and hence significantly more extended Lyα emission and absorption. However, unlike the deepest absorption feature in TN J1338-1942, the offset velocity of the absorption component 2 in MRC0943-242, is rather more modest, only a few $100\,\rm km\,s^{-1}$ compared to $1200\,\rm km\,s^{-1}$. Deeper data for MRC0934-242 may reveal a greater extent and more complex structure of the emitting and absorbing gas.

In addition to the ionisation cone and the general distribution of the Lyα emission around the central regions of Yggdrasil ($M_* \simeq 1.7 \times 10^{11}\,\rm M_{\odot}$), there is a bridge of material connecting the IRAC continuum emission of Thor and beyond ($M_* \simeq 1.0 \times 10^{11}\,\rm M_{\odot}$). Ivison et al. (2008) also found multiple components for the HzRG 4C60.07 at $z = 3.8$, likewise connected by a bridge of gas. They interpret this bridge as a plume of cold dust and gas in a tidal stream between two interacting galaxies. The interaction between the two galaxies is believed to be the trigger of the starburst and through this exhaust the molecular gas supply in the AGN host galaxy. One scenario which could have triggered the high star formation in Freja, Thor and Odin and perhaps the AGN activity in Yggdrasil is, like for 4C60.07, interaction between two galaxies. In this scenario, the two galaxies interact tidally where gas flows between the galaxies trigger the AGN activity in Yggdrasil, and creates tidal tails of gas which may emit Lyα. The tidal interactions may then ignite the string of components Freja, Thor and Odin resulting in a SFR ∼ 1400 $\rm M_{\odot}$/yr. However, the CO(8–7) emission line from Yggdrasil is very narrow and dynamically quiescent. It shows no signs of dynamical motion, implying that this gas is not related to the tidal interaction. The CO gas appears to be quite highly excited, as may be expected for gas near the central AGN. However, we remark that the ATCA upper limit on the CO(1-0) emission is rather shallow, so we cannot put strong constraints on the CO gas excitation.

Along the same projected line as the bridge and dust emitting regions, we find CO(8–7) emission in Loke which is not detected in any optical or dust continuum counterpart. The tentative detection of CO(1–0) at the position of Loke is consistent with the presence of a large reservoir of molecular gas. However, it is not clear from the observations at hand how extended this reservoir is, if it reaches across Freja, Thor, Odin and Loke, tracing one compact region, or if the reservoir is only at the location of Loke. The tentative CO(1-0) detection suggests a lower excitation level than Yggdrasil, but more sensitive low-J observations are needed to confirm this. The only thing known is that this region contains dynamically quiet but likely highly excited gas component ∼ 90 kpc away from the nearest stellar emission and with a relatively low velocity compared to the systemic velocity of the AGN. A clue to its nature lies in the alignment with the AGN and starburst components along the bridge. If this represents an accretion flow of galaxies and material along this direction, the gas would experience tidal forces and accretion shocks when the galaxies get close (or enter the halo of Yggdrasil). The absorption component 2 reveals the presence of a large amount of neutral gas at a radius > 60 kpc from the AGN, however the impact on this gas from merging galaxies or accreting gas is unknown. It may be that as gas enters the halo, it will encounter the large scale neutral gas, perhaps shocking it as it penetrates.

Mass	Yggdrasil $M_\odot$	Freja/Thor/Odin/Loke $M_\odot$
$M_{stellar}$	1.7×10^{11}	1×10^{11}
M_{ion}	5.2×10^{8}	—
$M_{neutral}$	3.8×10^{9}	—
M_{mol}	6×10^{10}	2.3×10^{10}

Table 6. The stellar mass, ionised-, neutral- and molecular gas mass for Yggdrasil and Thor.

Only more sensitive studies of the molecular gas in Loke may this impact be revealed.

4.2. Distribution of masses

To understand the nature of the MRC0943-242 system, it is important to know how the mass is distributed in the system. Following De Breuck et al. (2003), we estimate the ionised gas masses of Yggdrasil. The mass of the ionised gas is given by $M_{\rm ion} = 10^9 (f_{-5} L_{44} V_{70})^{1/2}\,{\rm M}_\odot$, where f_{-5} is the filling factor in units of 10^{-5}, L_{44} is the Lyα luminosity in units of 10^{44} erg/s and V_{70} is the volume in units of 10^{70} cm^3. We assume a filling factor of 10^{-5} (McCarthy et al. 1990) and a volume of $5'' \times 2.5'' \times 2.5''$, and therewith find $M_{\rm ion} = 5.2 \times 10^8\,{\rm M}_\odot$. This is a lower limit to the total mass since the absorption in the Lyα emission is significant. Since the distribution of the absorption components 1, 3, and 4 are only delineated by the Lyα emission, it is unknown how this gas is distributed, meaning we are most likely underestimating their column densities as the components do not fully cover the emission. This means we cannot estimate their contributions to the mass budget.

Absorption component 2 is observed in all the Lyα line profiles across the Lyα emitting regions and must therefore cover the entire Lyα emitting region out to at least ~ 60 kpc. Assuming it is distributed as a spherical shell, we estimate the total mass of absorption component 2 again following De Breuck et al. (2003), $M_{\rm neutral} \gtrsim 3.8 \times 10^9 (R/60\,{\rm kpc})^2 (N_{\rm HI}/10^{19})\,{\rm cm}^{-2}\,{\rm M}_\odot$, where R is the radius of the neutral gas and $N_{\rm HI}$ is the HI column density. We note that because the absorption is heavily damped (Jarvis et al. 2003), our column density estimate is likely a lower limit of the true column, and our mass estimate therefore a lower limit.

Using the tentative CO(1–0) detection at the position of Loke, and choosing a conservative $\alpha_{\rm CO} = 0.8\,{\rm M}_\odot\,{\rm K\,km\,s^{-1}\,pc^{-2}}$ (Downes & Solomon 1998) we estimate a molecular gas mass of $2.3 \times 10^{10}\,{\rm M}_\odot$ for Loke. Emonts et al. (2011) discovered a tentative 3σ CO(1–0) detection ~ 60 kpc North-East of Yggdrasil, and estimate a molecular gas mass of $M_{\rm H_2} = 6 \times 10^{10}\,{\rm M}_\odot$, using the same value for $\alpha_{\rm CO}$.

It is clear from comparing the four mass estimates (Table 6) that the most of the mass is in the form of stars and molecular gas, although the contribution of the neutral shell of gas may also be significant.

4.3. Ionisation mechanism

The high ionisation lines such as HeII, CIV, and CIII] are extended beyond the western lobe and asymmetric on large scales (see panel A-C of Fig. 7). The simplest interpretation is a strong asymmetry in the gas distribution. This hypothesis is supported by the hard photons, which are most likely responsible for the ionisation of the gas, causing the asymmetry in the emission from the circum-nuclear gas. Moreover, the ALMA data show a similar asymmetry in the distribution of both the dust and CO emission. However, this emitting gas lies outside of the ionisation cone and can therefore not be affected.

The detected emission lines from Lyα, CIV, HeII, CIII] and CII] can be used as probes for the ionisation mechanisms. Both the AGN and the far-UV field of vigorous star-formation can ionise the gas. The line ratios of Lyα, CIV and HeII can be used to determine the contribution from stellar photoionisation (Fig. 4 of Villar-Martín et al. (2007)). We find that the observed (absorption corrected) line ratios of Yggdrasil (Table 1) are consistent with $\omega = 0$, i.e. pure AGN photo-ionisation. Similarly, we can use the CIV/HeII, CIII]/HeII, CIV/CIII], CII]/CIII], CIV/Lyα and CIII]/Lyα flux ratios along with the diagrams of De Breuck et al. 2000 (their Fig. 13, adapted in Fig A.1). This comparison shows that the gas within the radio lobes of Yggdrasil, is likely ionised by a combination of photo-ionisation ($\sim$70%) and shock + precursors ($\sim$30%). CII] emission is an especially sensitive tracer of shock-ionised gas (Best et al. 2000; De Breuck et al. 2000). Our MUSE data allow us to produce a CII] narrow-band (moment-0) image (see panel D of Fig. 7). Interestingly, this image indeed reveals that the CII] emission is confined within the radio lobes, as would be expected if this line is dominated by shock ionised gas. Deeper MUSE data would be needed to check if this is not just due to limited S/N. This also limits us to derive line ratios in the extended halo (near Bifrost), where we detect Lyα, but no other emission lines. Deeper data would allow to check if the gas at ~ 80 kpc is still ionised by the AGN, or has a more important contribution from stellar photo-ionisation or shocks.

4.4. AGN and starbursts

Disentangling the SED into several components suggests that the starburst activity in HzRGs is driven by the interaction of two (or more) gas-rich systems. Major mergers have been invoked to explain the high SFRs seen in submm galaxies (SMGs; e.g. Engel et al. 2010), though others argue that they may rather represent the top end of a "main sequence" of star-forming galaxies (e.g. Michałowski et al. 2012). The similar morphologies and stellar masses of HzRGs and SMGs suggest they may be related, potentially through an evolutionary sequence, a high-z extension of the local relation between QSOs and ULIRGs (Sanders et al. 1988). Both classes reside in parent halos of similar mass (Hickox et al. 2012), but direct observations of objects in transition between SMGs and QSOs remain restricted to a few examples (e.g. Simpson et al. 2012). This is where detailed observational studies of type 2 AGN like HzRGs can play an important role, as their stellar masses, unlike type 1 AGN's, can be accurately determined (Seymour et al. 2007; De Breuck et al. 2010).

In MRC0943-242, we actually observe both processes: in Yggdrasil, we observe an AGN host galaxy with a moderate SFR, while the companion galaxy Thor is surrounded by two additional star-forming companions, Odin and Freja.

4.5. Loke is not so atypical around radio galaxies

Our detection of CO(8–7) emission in Loke, which is not coincident with any dust or stellar emission, and is not in the direction of the axis of the radio emission, is puzzling. It is not the first time CO line emission has been detected around a HzRG without any counterpart at other wavelengths. Table 7 lists ten HzRG with CO observations where the CO emission is offset from the AGN compared to the radio sources.

Nesvadba et al. (2009) found CO(3–2) emission 80 kpc from the core of the $z = 2.6$ HzRG TXS0828+193. However, the

HzRG	z	CO detection	Separation[a]	CO/dust association	Reference
MRC0114-211	1.402	CO(1–0)	35 kpc	no	Emonts et al. (2014); Nilsson et al. in prep.
MRC0152-209	1.921	CO(1–0)/CO(6–5)	10 kpc	yes	Emonts et al. (2014, 2015)
MRC0156-252	2.016	CO(1–0)	60 kpc	no	Emonts et al. (2014); Nilsson et al. in prep.
MRC2048-272	2.060	CO(1–0)	55 kpc	no	Emonts et al. (2014); Nilsson et al. in prep.
MRC1138-262	2.161	CO(1–0)	30-40 kpc	yes	Emonts et al. (2013); Gullberg et al. in prep.
TXS0828+193	2.572	CO(3–2)	80 kpc	no	Nesvadba et al. (2009)
MRC0943-242	2.923	CO(8–7)	80 kpc	no	*This work*
B3J2330+3927	3.086	CO(1–0)/CO(4–3)	30 kpc	yes	Ivison et al. (2012)
4C41.17	3.798	CO(4–3)	13 kpc	yes	De Breuck et al. (2005)
4C60.07	3.8	CO(1–0)/CO(4–3)	30 kpc	yes	Ivison et al. (2008); Greve et al. (2004)

Table 7. Overview of CO detections that are not directly associated with the radio galaxy. *a*: Separation between the AGN and the CO detection.

CO(3–2) emission in TXS0828+193 is aligned with the radio jet, which Nesvadba et al. (2009) suggest could be triggering the collapse and excitation of the gas. The offset of CO emission from the position of the HzRG is seen in other sources as well (see Table 7) such as, e.g. 4C60.07 (Ivison et al. 2008), MRC0114-211, MRC0156-252 and MRC2048-272 (Emonts et al. 2014). Ivison et al. (2008) detect CO(4–3) emission for the HzRG at $z = 3.8$ at two positions: at the location of the AGN core and 7″ SW of the AGN. The latter component is also detected in CO(1–0) emission (Greve et al. 2004). Based on the submm observations of 4C60.07, Ivison et al. (2008) point out a complication when calculating dynamical masses using the extended CO emission, due to the misalignment of the black hole with the CO emission and dust continuum. Emonts et al. 2014 discovered CO(1–0) emission in three HzRGs that were significantly offset from the AGN and which have 4.5-9.2×10^{10} $M_\odot$ of molecular gas, but again aligned with the radio jet. They discuss jet-induced star formation. Two molecular components traced by CO(4–3) for 4C41.17 were detected by De Breuck et al. 2005. These two components are also aligned with the radio jet, but are co-spatial with the Lyα emission.

The submm and optical observations of MRC 0943-242, adds to this complicated situation, with its many components, only two of which are traced by CO emission.

5. Are we seeing a multiphase accretion flow?

Numerical simulations suggest that galaxies acquire much of their gas through accretion flows generated by the growth of the cosmic web of dark matter (e.g. Agertz et al. 2011; Danovich et al. 2015). Flows of gas develop over cosmological distances and time scales, ultimately penetrating into halos and feeding baryons onto galaxies. Because the flows are associated with the growth of dark matter structures, galaxies are expected to be embedded in accretion flows. Could we be witnessing such accretion in our combined data sets?

Progressing inwards in radius towards the host galaxy of MRC 0943-242 over many 10s of kpc from Loke, through Odin, Thor, Freja, Bifrost to the redshifted absorption component 3 seen against the inner Lyα emission, we see little change in the velocity over this inward journey. In the most distant emission, i.e. Loke, the velocity offset relative to the AGN emission is small. This structure appears dynamically cold, having low dispersion in all of its spectroscopic features, implying that it is near to the plane of the sky. Aligned with this general structure is a group of (merging?) vigorous star-forming galaxies associated with the emission regions, Freja, Thor and Odin. If the coincident Lyα emission from Bifrost is representative of their projected velocity, these galaxies are embedded within this overall (in projection) linear structure. On the opposite end of the structure, we find the AGN host galaxy, Yggdrasil, which has a rather mundane rest-frame optical morphology, suggesting a heavily obscured galaxy, but not a merger (see Fig. 9 of Pentericci et al. 2001). Interestingly, the extended emission line halo does not extend on the other side of the AGN.

Admittedly, we do not have a simple explanation for the distribution of the various phases. For example, why is most of the molecular gas observed at the position of Loke? An explanation could be that the molecular gas is related to the strong, optically thick, large covering fraction of HI absorption component 2. However, the velocity offsets (Fig. 4) suggest that it is rather the less massive absorption component 3 that coincides with the CO(8-7) and simply part of what may be a flow into Yggdrasil.

Only a combined ALMA + MUSE survey of radio galaxies like that of MRC0943-242 (with deeper integrations than in this pilot project) can determine if it is gas accretion that is fuelling the growth of their galaxies and supermassive black-holes. These combined data cubes are our only way to obtain a complete picture of various phases which emit strongly over a wide range of wavelengths. This will allow us to study the nature of the halo gas that results from this complex interaction. By the sensitivity of both ALMA and MUSE on the VLT are already offering tantalising clues on how the gas in this system is being acquired and modified by the interaction with the AGN and galaxies in this complex system.

6. Conclusions

Combining the high sensitivity of ALMA and MUSE, even with very modest integration times, has allowed us to gain insights into the environments which explain many properties of the evolutionary path of HzRGs. Surprisingly, in our pilot study of the $z = 2.9$ radio galaxy MRC0943-242, we apparently find that most of the star formation is not associated with the radio galaxy itself, but is in a companion set of galaxies which exhibits a complex pattern of dust emission which we associate with star formation. We say apparently, because the morphology of the dust emission is peculiarly distributed in three distinct sources but roughly within the diffuse stellar continuum emission of the source.

The MUSE data show that the continuum emitting source is embedded in a Lyα emitting linear filament stretching from beyond the AGN to the circum-nuclear emission of the AGN. This structure of dust and Lyα emission aligns well in projection with a region of CO(8–7) and CO(1–0) emitting gas (at lower significance) about 90 kpc in projection from the AGN.

The AGN apparently ionises a large region which is asymmetric, lying mostly on the western side of the source. This is

likely due to the gas distribution as it tantalisingly lies in the direction where the dust, CO line emission, and the filamentary Lyα emission are found.

The relationship between the Lyα emission and absorption and the associate CIV absorption, paint a fascinating picture of the distribution of the warm ionised medium. There is a component of Lyα absorbing gas which reaches zero intensity throughout the Lyα emission detected across MRC0943-242 in the MUSE data. It clearly has a unity covering fraction and is highly optically thick. Since the gas is seen as an absorption feature throughout the Lyα emitting filament (Bifrost) this thick, unity covering fraction absorber is extended, and visible in absorption out to $>$ 60 kpc. Because of its velocity and optical thickness, it literally absorbs all of the extended Lyα emission in the cube.

Appendix A: Line ratio diagrams from De Breuck et al. 2000

This appendix presents a range of emission line ratio diagrams that are directly derived from the MUSE data, compared photo-ionization and shock ionization models (Fig. 13 from De Breuck et al. 2000).

Acknowledgements. We thank the anonymous referee for her/his very thorough reading of our manuscript, and suggestions that substantially improved our paper. This publication uses data taken from the MUSE commissioning run 060.A-9100. All of the MUSE data used in this paper are available through the ESO science archive. This paper makes use of the following ALMA data: ADS/JAO.ALMA#2012.1.00039.S. ALMA is a partnership of ESO (representing its member states), NSF (USA) and NINS (Japan), together with NRC (Canada) and NSC and ASIAA (Taiwan), in cooperation with the Republic of Chile. The Joint ALMA Observatory is operated by ESO, AUI/NRAO and NAOJ. The work of DS was carried out at Jet Propulsion Laboratory, California Institute of Technology, under a contract with NASA. BE acknowledges funding through the European Union FP7 IEF grant nr. 624351. MDL acknowledges the support from the ESO visitors program and especially would like to thank Mario van den Ancker for his help and Eric Emsellem for interesting scientific discussions. Nick Seymour is the recipient of an ARC Future Fellowship.

References

Agertz, O., Teyssier, R., & Moore, B. 2011, MNRAS, 410, 1391
Archibald, E. N., Dunlop, J. S., Hughes, D. H., et al. 2001, MNRAS, 323, 417
Bacon, R., Accardo, M., Adjali, L., et al. 2010, in Society of Photo-Optical Instrumentation Engineers (SPIE) Conference Series, Vol. 7735, Society of Photo-Optical Instrumentation Engineers (SPIE) Conference Series, 8
Bacon, R., Vernet, J., Borisova, E., et al. 2014, The Messenger, 157, 13
Bekki, K. 1998, ApJ, 504, 50
Best, P. N., Röttgering, H. J. A., & Longair, M. S. 2000, MNRAS, 311, 23
Binette, L., Kurk, J. D., Villar-Martín, M., & Röttgering, H. J. A. 2000, A&A, 356, 23
Carilli, C. L., Röttgering, H. J. A., van Ojik, R., et al. 1997, ApJS, 109, 1
Danovich, M., Dekel, A., Hahn, O., Ceverino, D., & Primack, J. 2015, MNRAS, 449, 2087
De Breuck, C., Downes, D., Neri, R., et al. 2005, A&A, 430, L1
De Breuck, C., Neri, R., Morganti, R., et al. 2003, A&A, 401, 911
De Breuck, C., Röttgering, H., Miley, G., van Breugel, W., & Best, P. 2000, A&A, 362, 519
De Breuck, C., Seymour, N., Stern, D., et al. 2010, ApJ, 725, 36
De Breuck, C., van Breugel, W., Stanford, S. A., et al. 2002, AJ, 123, 637
Downes, D. & Solomon, P. M. 1998, ApJ, 507, 615
Drouart, G., De Breuck, C., Vernet, J., et al. 2014, A&A, 566, A53
Eales, S., Rawlings, S., Law-Green, D., Cotter, G., & Lacy, M. 1997, MNRAS, 291, 593
Emonts, B. H. C., De Breuck, C., Lehnert, M. D., et al. 2015, ArXiv e-prints
Emonts, B. H. C., Feain, I., Röttgering, H. J. A., et al. 2013, MNRAS, 430, 3465
Emonts, B. H. C., Norris, R. P., Feain, I., et al. 2014, MNRAS, 438, 2898
Emonts, B. H. C., Norris, R. P., Feain, I., et al. 2011, MNRAS, 415, 655
Engel, H., Tacconi, L. J., Davies, R. I., et al. 2010, ApJ, 724, 233
Greve, T. R., Ivison, R. J., & Papadopoulos, P. P. 2004, A&A, 419, 99
Hickox, R. C., Wardlow, J. L., Smail, I., et al. 2012, MNRAS, 421, 284
Ivison, R. J., Morrison, G. E., Biggs, A. D., et al. 2008, MNRAS, 390, 1117
Ivison, R. J., Smail, I., Amblard, A., et al. 2012, MNRAS, 425, 1320
Jarvis, M. J., Wilman, R. J., Röttgering, H. J. A., & Binette, L. 2003, MNRAS, 338, 263
Kennicutt, Jr., R. C. 1998, ApJ, 498, 541
Laurent, G. T., Aguirre, J. E., Glenn, J., et al. 2005, ApJ, 623, 742
Lilly, S. J. & Longair, M. S. 1984, MNRAS, 211, 833
McCarthy, P. J., Spinrad, H., Dickinson, M., et al. 1990, ApJ, 365, 487
Michałowski, M. J., Dunlop, J. S., Cirasuolo, M., et al. 2012, A&A, 541, A85
Mullaney, J. R., Alexander, D. M., Goulding, A. D., & Hickox, R. C. 2011, MNRAS, 414, 1082
Nesvadba, N. P. H., Neri, R., De Breuck, C., et al. 2009, MNRAS, 395, L16
Ogle, P., Whysong, D., & Antonucci, R. 2006, ApJ, 647, 161
Pentericci, L., McCarthy, P. J., Röttgering, H. J. A., et al. 2001, ApJS, 135, 63
Reuland, M., Röttgering, H., van Breugel, W., & De Breuck, C. 2004, MNRAS, 353, 377
Reuland, M., van Breugel, W., Röttgering, H., et al. 2003, ApJ, 592, 755
Röttgering, H. J. A., Hunstead, R. W., Miley, G. K., van Ojik, R., & Wieringa, M. H. 1995, MNRAS, 277, 389
Sanders, D. B., Soifer, B. T., Elias, J. H., et al. 1988, ApJ, 325, 74
Seymour, N., Altieri, B., De Breuck, C., et al. 2012, ApJ, 755, 146
Seymour, N., Stern, D., De Breuck, C., et al. 2007, ApJS, 171, 353
Simpson, C., Rawlings, S., Ivison, R., et al. 2012, MNRAS, 421, 3060
Swinbank, A. M., Vernet, J. D. R., Smail, I., et al. 2015, MNRAS, 449, 1298
Tremaine, S., Gebhardt, K., Bender, R., et al. 2002, ApJ, 574, 740
van Breugel, W. J. M., Stanford, S. A., Spinrad, H., Stern, D., & Graham, J. R. 1998, ApJ, 502, 614
van Ojik, R., Roettgering, H. J. A., Carilli, C. L., et al. 1996, A&A, 313, 25
Venemans, B. P., Röttgering, H. J. A., Miley, G. K., et al. 2007, A&A, 461, 823
Vernet, J., Fosbury, R. A. E., Villar-Martín, M., et al. 2001, A&A, 366, 7
Villar-Martín, M., Humphrey, A., De Breuck, C., et al. 2007, MNRAS, 375, 1299
Villar-Martín, M., Vernet, J., di Serego Alighieri, S., et al. 2003, New A Rev., 47, 291
Weilbacher, P. M., Streicher, O., Urrutia, T., et al. 2012, in Society of Photo-Optical Instrumentation Engineers (SPIE) Conference Series, Vol. 8451, Society of Photo-Optical Instrumentation Engineers (SPIE) Conference Series, 0
Weiß, A., Downes, D., Neri, R., et al. 2007, A&A, 467, 955
Wylezalek, D., Galametz, A., Stern, D., et al. 2013, ApJ, 769, 79

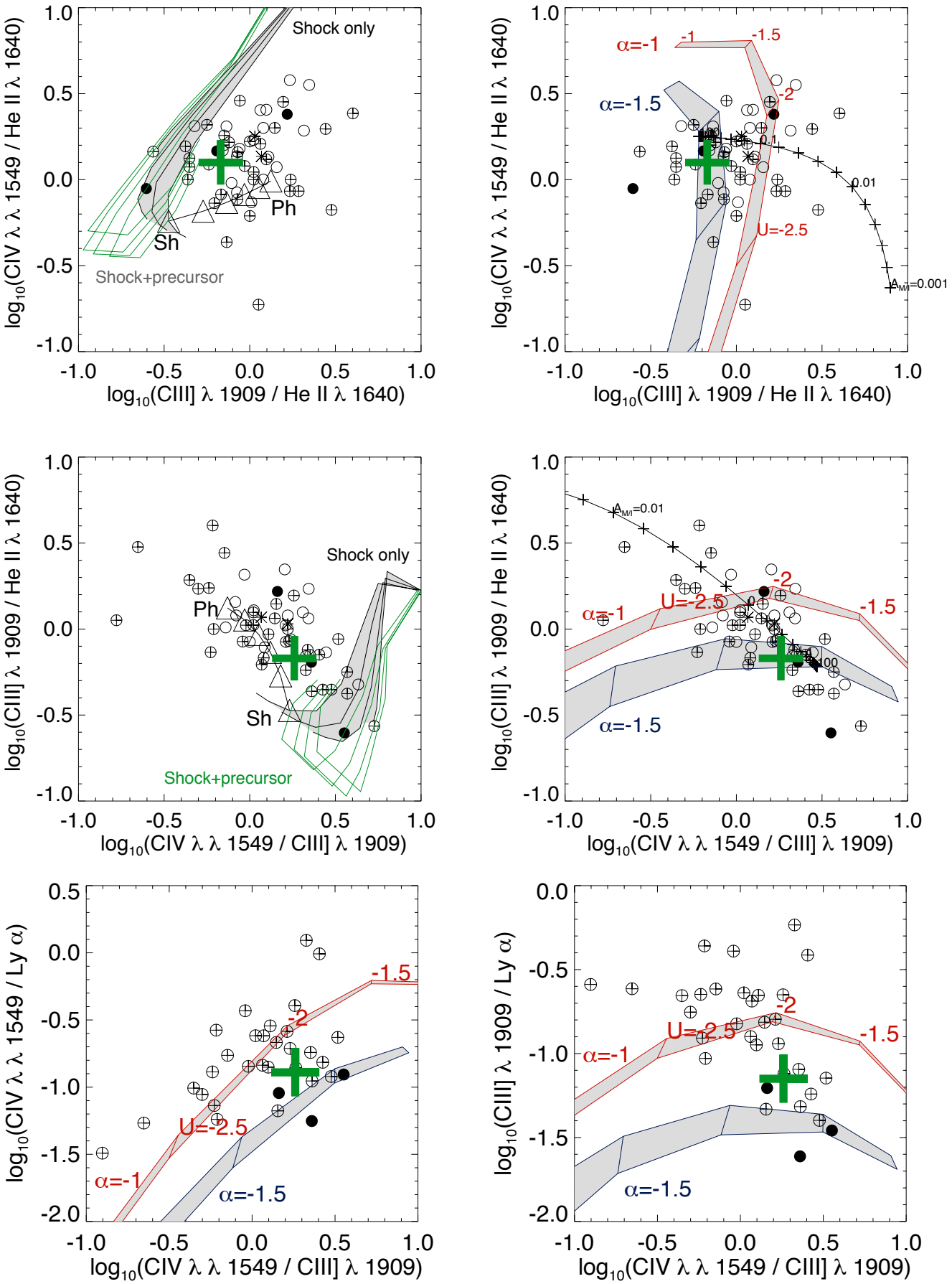

Fig. A.1. Line ratio diagnostic diagrams involving Lyα, CIV, HeII, CIII] and CII] (adapted from De Breuck et al. 2000, their Fig. 13). The thick green cross shows the flux line ratios observed for Yggdrasil, while the circles show other HzRGs from the literature. Also shown are photo-ionization and shock models to illustrate that the observed line ratios in Yggdrasil are dominated by photo-ionization with a contribution of up to ~30% by shocks (see De Breuck et al. 2000, for more details).